Mechanics & Industry **27**, 18 (2026)
© L. Yuan et al., Published by EDP Sciences, 2026
https://doi.org/10.1051/meca/2026012

Mechanics & Industry

Available online at:
www.mechanics-industry.org

Original Article — Open Access

Hydrogen-bond regulated NADES lubricants enable ultra-low wear in high-speed ball screw pairs

Lei Yuan[1,★], Zhaoyang Wang[2,★], Changguang Zhou[1], Michel Fillon[3], Meng Wang[1], Yibiao Wang[1], Bi Wentao[2,*], and Wenling Zhang[1,*]

[1] School of Mechanical Engineering, Nanjing University of Science and Technology, Nanjing 210094, PR China
[2] Jiangsu Collaborative Innovation Center of Biomedical Functional Materials, Jiangsu Key Laboratory of Biomedical Materials, College of Chemistry and Materials Science, Nanjing Normal University, 1 Wenyuan Road, Nanjing 210023, PR China
[3] Retired from Pprime Institute, CNRS, University of Poitiers, TSA 41123, 86073 Poitiers Cedex, France

Received: 4 January 2026 / Accepted: 27 February 2026

Abstract. Ball screw pairs are susceptible to severe friction and wear under harsh operating conditions, particularly high loads and high speeds, which compromise positioning accuracy and transmission stability. To address these challenges, this study develops a novel green lubricant based on natural deep eutectic solvents (NADESs), which exhibit high load-carrying capacity and stable lubrication performance. Experimental results reveal that the dense hydrogen bond network within NADESs restricts molecular mobility, thereby enhancing film stability. A robust tribofilm is formed through the synergistic mechanism of physicochemical adsorption and tribochemical reactions, resulting in significantly smoother worn surfaces. Compared to the commercial lubricant PAO40, the proposed NADESs reduced the friction coefficient and wear volume by 32.6% and 89.1%, respectively. Furthermore, friction torque tests on ball screw pairs demonstrated that NADESs exhibit superior lubricity and significantly improved motion stability even at high rotational speeds. Consequently, the formulated NADESs show great potential as high-performance green alternatives for precision transmission systems requiring high load-bearing capacity.

Keywords: Natural deep eutectic solvents / green lubricants / hydrogen bonding / ball screw pair / friction and wear

1 Introduction

Ball screw pairs are characterized by high transmission efficiency, superior synchronization, and excellent capabilities for high-precision and high-sensitivity transmission [1]. Consequently, they are extensively utilized in precision CNC machine tools. To ensure the stable and efficient operation of these components, lubricants are applied to the contact interface between the ball and the raceway to reduce friction and torque. However, inadequate lubrication leads to an increase in friction torque, thereby deteriorating the motion stability of the ball screw pair.

Ball screw pairs in high-precision machine tools are frequently subjected to severe operating conditions, such as high speeds, heavy loads, and instantaneous impact loads, which impose stringent requirements on lubricant performance. On the one hand, under high speeds and high contact stresses, it is imperative to maintain a uniform and stable lubricating film to prevent lubrication failure caused by film rupture due to insufficient load-carrying capacity, which would otherwise compromise the reliability of the transmission system. On the other hand, driven by escalating environmental pollution concerns and growing environmental awareness, higher requirements for the environmental compatibility of lubricants have been established, which has become an inevitable development trend of lubrication technology in the future. Nevertheless, current lubricants predominantly rely on mineral base oils derived from petroleum refining, which presents significant drawbacks. First, mineral base oils exhibit poor biodegradability and inherent toxicity. Second, during use and disposal, they pose a high risk of causing persistent pollution to soil and water bodies, directly threatening ecological security and human health.

In recent years, deep eutectic solvents (DESs) have garnered significant attention as a novel category of green solvents and functional fluids [2–4]. Typically formed by combining a hydrogen bond donor (HBD) and a hydrogen bond acceptor (HBA), DESs exhibit melting points significantly lower than those of their individual

---

[*] e-mail: wlzhang@njust.edu.cn; biwentao@njnu.edu.cn
[★] These two authors contributed equally to this work.

components, a phenomenon attributed to the formation of extensive hydrogen-bonding networks [5–9]. DESs are characterized by exceptional physicochemical properties, such as facile and scalable synthesis [10], negligible vapor pressure [11], non-flammability, tunable polarity [12], and excellent thermal [13] and chemical stability [14]. These attributes have propelled their application in diverse fields, including electrochemistry [15], catalysis [16], biomass valorization [17], and separation science [18].

Moreover, DESs have demonstrated significant potential as sustainable lubricants. In a pioneering study in 2010, Lawes et al. [19] first proposed choline chloride (ChCl)–urea and ChCl–ethylene glycol DESs for lubricating steel contacts, finding that the coefficient of friction (COF) was comparable to that of fully formulated SAE 5W-30 engine oil. Following this study, researchers began to extensively explore the tribological behavior of various DESs under diverse conditions. For instance, Shi et al. [20] evaluated the lubrication performance of ChCl–urea, ChCl–ethylene glycol, and ChCl–1,2-propanediol DESs for carbon fiber-filled PTFE composites. Their results demonstrated that DESs outperformed both water and hydraulic oil, reducing the COF and wear by approximately 60% and 50%, respectively, compared to dry friction. Hallett et al. [21] further showed that a ChCl–ethylene glycol DES (1:2 molar ratio) could form a stable boundary film on mica surfaces, thereby enhancing lubrication. Li et al. [22] synthesized two hydrophobic DESs—tetrabutylammonium chloride-decanoic acid (C4-DES) and methyl trialkylmethylammonium chloride-decanoic acid (C8-DES) —and reported that compared to ester-based oils, these DESs significantly reduced COF (by 29% and 36%) and wear (by 91% and 94%, respectively). Despite these promising advancements, current tribological research on DESs remains unsystematic. Furthermore, existing studies have predominantly focused on specific DES formulations, leaving the influence of varying HBAs and HBDs on tribological behavior insufficiently explored. As a subclass of DESs, natural deep eutectic solvents (NADES) are derived from renewable resources such as sugars, amino acids, organic acids, and choline or betaine. Many studies [23,24] have shown that low melting point solvents composed of natural components such as choline chloride, urea, glycerol, etc. have high biodegradability and low toxicity, making them ideal candidates for the next generation of green lubricants.

As illustrated in Figure 1, this study tailored the hydrogen bond interactions by selecting specific HBDs and HBAs to synthesize five representative NADESs. First, through comprehensive physicochemical and tribological assessments, we determined how hydrogen bond strength influences the behavior of these NADESs. Second, by establishing the structure–property relationship between molecular composition and tribological performance, the mechanisms by which hydrogen bonding networks govern film formation, surface interactions, and lubrication were elucidated. Finally, the proposed NADESs were experimentally on ball screw pairs to assess their dynamic lubrication performance at varying speeds. This work provides critical insights for enhancing the transmission accuracy and long-term operational reliability of ball screws, holding significant value for the advancement of high-performance, eco-friendly next-generation lubricant.

2 Materials and experimental methods

2.1 Materials

Choline chloride, urea, betaine, malic acid, and anhydrous ethanol employed were purchased from Shanghai Aladdin Biochemical Technology Co., Ltd. Betaine and L-carnitine were purchased from Shanghai McLean Biochemical Technology Co., Ltd., with a purity greater than 99%. All reagents were used as received without further purification. A commercial base oil, specifically poly alpha olefin (PAO40; supplied by Tiancheng Meijia, PR China), was selected as a reference. Its frictional performance was comparatively analyzed against that of the NADESs.

2.2 Synthesis of NADESs

As detailed in Table S1, the specific HBAs and HBDs were weighed in a molar ratio of 1:2 and placed into sealed glass containers. The mixtures were heated to 80 °C and stirred at 400 rpm for approximately 1.5 min until homogeneous, transparent liquids were formed. The synthesized solvents are denoted as NADES-1 (ChCl–glycerol), NADES-2 (ChCl–urea), NADES-3 (ChCl–malic acid), NADES-4 (betaine–glycerol), and NADES-5 (L-carnitine–glycerol). For brevity, these abbreviations are used throughout the subsequent text.

2.3 Characterization of NADESs

Thermogravimetric analysis (TGA) and differential scanning calorimetry (DSC) were conducted using a TG-DSC 3+ thermal analyzer (Mettler Toledo, Switzerland). TGA was performed from 20°C to 600°C at a heating rate of 10°C/min under a nitrogen atmosphere, while DSC was carried out from -80°C to 100°C at the same heating rate. Approximately 30 mg of the test substance was dissolved in 1 mL of DMSO (99.9%) in a 5-mm NMR tube. ^{1}H-NMR spectra were obtained on a Bruker Avance III 400 MHz spectrometer equipped with a 5-mm BBFOZ gradient intelligent probe, and data processing was performed using MestReNova software. Contact angles of the NADESs on 45# steel substrates were measured using a DSA30S drop shape analyzer (KRUSS, Germany). ATR-FTIR spectra were acquired using a Spectrum 3 spectrometer (PerkinElmer, USA) in the scanning range of 650–4000 cm^{-1} with an accumulation of 20 scans. The dynamic viscosities of the five NADESs were measured at 20°C using an MCR302 rotational rheometer (Anton Paar, Austria) equipped with a CP20 cone-plate geometry.

2.4 Calculation of intermolecular interaction energy

Quantum mechanical calculations were performed to elucidate the intermolecular interactions. All computations were carried out using the Gaussian 09 software

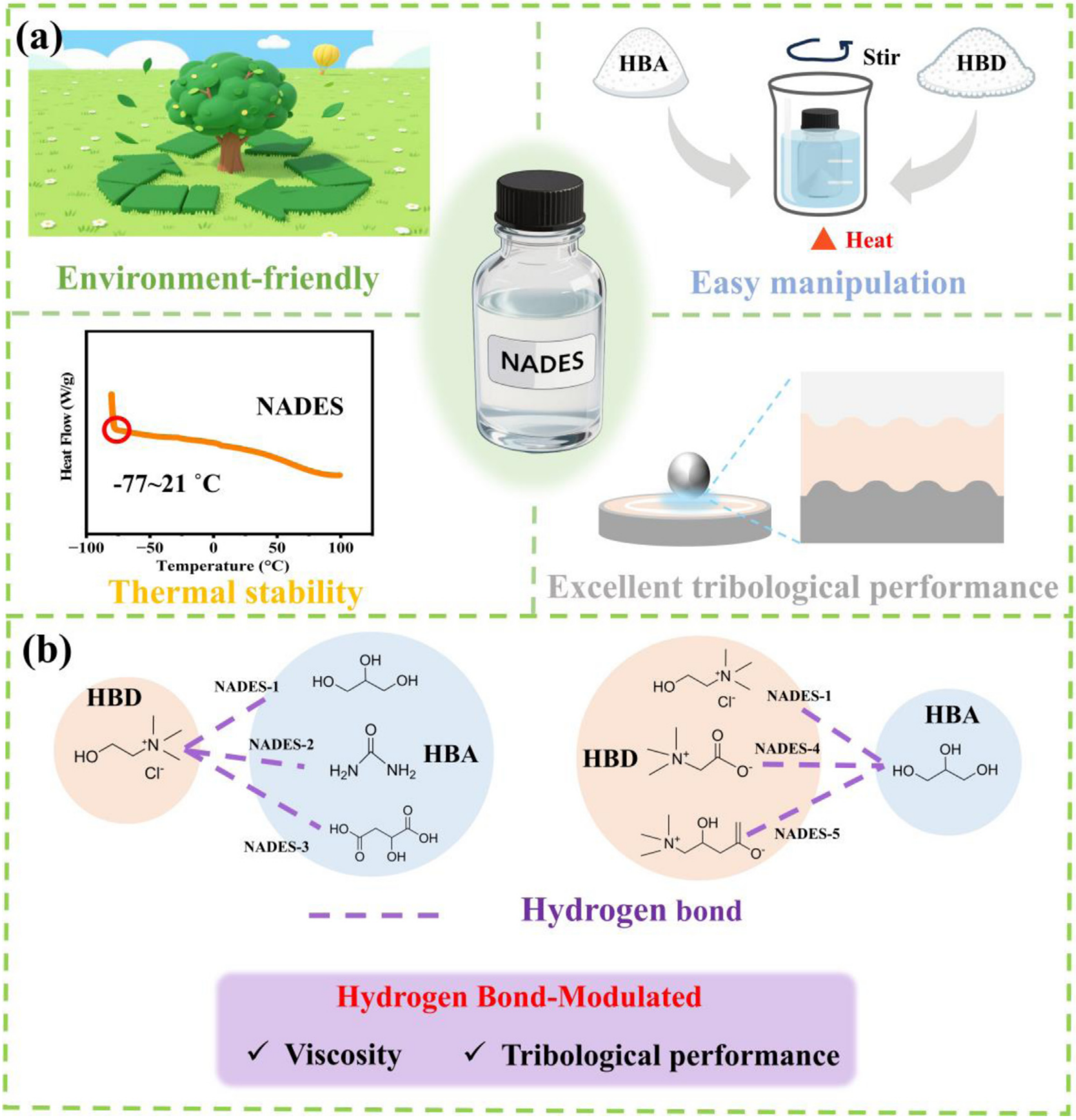

Fig. 1. (a) Characteristics of NADESs. (b) The NADESs studied in this study include NADES-1 (ChCl–glycerol), NADES-2(ChCl–urea), NADES-3(ChCl–malic acid), NADES-4 (betaine–glycerol), and NADES-5(L-carnitine–glycerol).

package. The M06-2X [25] functional and the 6-31 + G(d) basis set were employed for geometry optimization and single-point energy calculations. The electrostatic potential (ESP) distribution on the molecular surfaces was analyzed using the Multiwfn 3.8 program. The interaction energy was calculated according to the following formula:

$$E_{\mathrm{int}} = E_{\mathrm{A-B}} - E_{A} - E_{\mathrm{B+}}E_{\mathrm{BSSE}}, \tag{1}$$

where E_{int} represents the interaction energy, A and B represent individual molecules, A–B represents the complex formed following the interaction between A and B, and E_{BSSE} represents the basis set superposition error. E_{BSSE} is the basis set superposition error correction, calculated via the counterpoise method. After the formation of hydrogen bonds, the total energy of the complex (A–B) is lower than the sum of the energies of A and B, so the value of E_{int} is negative.

2.5 Stability testing

To evaluate the corrosivity of the prepared NADESs, 45# steel specimens were subjected to static immersion tests. The polished and cleaned steel specimens were fully submerged in the NADESs at room temperature (20°C) for a duration of 7 days, during which optical images were captured daily to monitor surface changes. Furthermore, comparative FTIR analysis of the NADESs before and after the friction tests was conducted to investigate potential variations in the hydrogen-bonding network and chemical composition induced by the lubrication process.

2.6 Friction testing

The tribological performance of the NADESs was evaluated using a ball-on-disc tribometer (UMT-2, Bruker, USA) in rotary mode. The upper specimen was a GCr15 ball

($\Phi = 6.35$ mm, Ra = 30 nm), while the lower specimen was a 45# steel disc ($\Phi = 40$ mm). These materials were selected due to their extensive application in mechanical components [26]. The disc surfaces were polished sequentially using abrasive papers with grits of 100, 500, 1000, and 2000. Subsequently, the discs were cleaned with ethanol, and their surface roughness was measured using a white light interferometer, ensuring it was controlled within 20 nm. Prior to testing, both the steel balls and discs were ultrasonically cleaned in ethanol. The test parameters were set as follows: a rotation radius of 4 mm, a rotation speed of 60 rpm, and a duration of 30 min. The running-in time is 10 min. The COF was recorded continuously under varying normal loads of 50, 100, and 150 N, which correspond to initial maximum Hertzian contact stresses of 2.32, 2.93, and 3.35 GPa, respectively. The maximum Hertzian contact stress was calculated using the following equation:

$$\frac{1}{\pi}\sqrt{6F\left(\frac{\rho}{E}\right)^2}, \tag{2}$$

where F represents the applied pressure, ρ represents the equivalent radius of curvature, and E denotes the equivalent elastic modulus. The calculation formula for equivalent radius R and equivalent elastic modulus E is:

$$\begin{cases} \frac{1}{\rho} = \frac{1}{\rho_1} + \frac{1}{\rho_2}, \\ \frac{1}{E} = \frac{1-\upsilon_1^2}{E_1} + \frac{1-\upsilon_2^2}{E_2}. \end{cases} \tag{3}$$

Among them, ρ_1 and ρ_2, respectively, represent the principal curvature radius of the bearing steel ball and the 45# steel chassis at the contact point. E_1 and E_2, respectively, represent the Young's modulus of bearing steel and 45# steel. $\boldsymbol{\upsilon}_1$ and $\boldsymbol{\upsilon}_2$ represent the Poisson's ratio of bearing steel and 45# steel, respectively.

The cross-sectional area of the wear scar S is obtained using contour integration, and the calculation method is as follows:

$$S = \int_a^b A(x)dx. \tag{4}$$

Among them, a and b are the starting and ending coordinates in the width direction of the abrasion, respectively, and $A(x)$ is the contour function of the wear scar.

Assuming that the wear area of each section is consistent, the formula for calculating the wear volume V is as follows:

$$V = 2\pi R \times S. \tag{5}$$

Among them, R is the rotation radius in the friction lubrication experiment, and S is the wear cross-sectional area of the wear scar.

The experiments were conducted at a temperature of 20°C and a relative humidity of 50%. Each test was repeated at least three times to minimize random errors and ensure data reproducibility. We define the steady-state phase as the period from the 10th to the 30th min after the start of the friction coefficient test, and the experimental data during these 20 min are recorded. Additionally, it should be noted that all error bars in the figures represent the standard deviation.

2.7 Analysis of worn surfaces

Upon completion of the friction tests, the width and depth of the wear tracks were measured at three different locations using a white light interferometer (Verifire XL, ZYGO, USA) to calculate the average wear volume and wear rate. To elucidate the lubrication mechanisms of the NADESs, the morphology and chemical composition of the worn disc surfaces were analyzed. First, optical images of the wear tracks were acquired using an optical microscope (Smart Zoom 5, Zeiss, Germany). The surface morphology and elemental composition were then characterized using a field emission scanning electron microscope (FE-SEM, Gemini 300, Zeiss, Germany) equipped with energy-dispersive X-ray spectroscopy (EDS). Finally, X-ray photoelectron spectroscopy (XPS, K-Alpha, Thermo Fisher Scientific, USA) was employed to analyze the chemical states of the worn surfaces and investigate the formation of a tribofilm.

2.8 Friction torque tests of ball screw pair

The ball screw model employed in the experiments is the NSK4006-25T3, which features a single-nut configuration. The nominal diameter of the screw pair is 40 mm, the lead is 6 mm, and the effective stroke is 100 mm. The preload force of the ball screw is 1950 N. No axial load was applied during the experiment. With a nominal diameter of 40 mm, this model is classified as a large-scale, heavy-duty ball screw. It is characterized by high rigidity, superior bending resistance, and exceptional load-bearing capacity (capable of withstanding axial dynamic loads exceeding 60 kN), making it widely utilized in precision machine tools.

Prior to testing, the sealing rings were removed, and the original lubricating grease on the screw shaft, nut raceways, and ball surfaces was thoroughly cleaned using gasoline. Once the gasoline had completely evaporated, the ball screw pair was installed on the dynamic pre-tightening torque test bench. Following installation verification, the ambient conditions were strictly controlled, with the temperature maintained at 20 ± 1°C and relative humidity at 50 ± 5%. The test stroke was set to 100 mm. To ensure sufficient lubrication, first fill the nut space with 20 mL of lubricating oil and run the system in a reciprocating motion at 100 rpm for 3 cycles. No additional lubricant was added during each experiment. Subsequently, the forward and reverse dynamic friction torques were measured at various rotational speeds. One full reciprocating stroke constituted one data set. Measurements were repeated three times for each speed, and the average value was calculated to minimize random errors. Notably, due to the excessively high viscosity and mild acidity of NADES-3, it was excluded from these experiments.

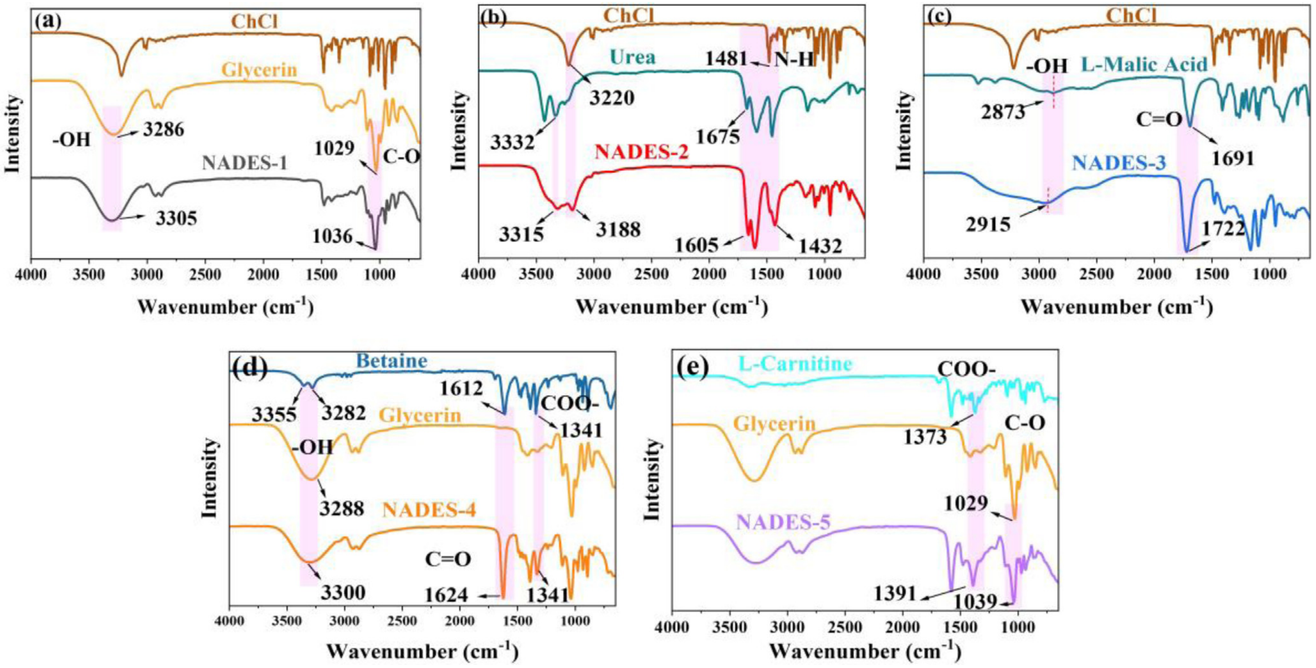

Fig. 2. FTIR spectra of (a) ChCl, glycerol, and NADES-1; (b) ChCl, urea, and NADES-2; (c) ChCl, malic acid, and NADES-3; (d) betaine, glycerol, and NADES-4; and (e) L-carnitine, glycerol, and NADES-5.

3 Results and discussion

3.1 Characterization of NADESs

The formation of hydrogen bonds and the successful synthesis of the five NADESs were confirmed by FTIR spectroscopy, as evidenced by characteristic peak shifts associated with functional group interactions [27]. Figure 2a illustrates the FTIR spectra of ChCl, glycerol, and NADES-1. The characteristic peaks at 3286 and 1029 cm^{-1} are attributed to the -OH and C-O groups of glycerol, respectively. In the spectrum of NADES-1, the hydroxyl (-OH) peak shifted to a higher wavenumber, appearing at 3305 cm^{-1}. Additionally, the C-O peak of glycerol exhibited a shift from 1029 to 1036 cm^{-1}. These observations demonstrate the formation of hydrogen bonds between ChCl and glycerol, indicating the successful synthesis of NADES-1. Figure 2b presents the spectra of ChCl, urea, and NADES-2. The peaks at 1675 and 1589 cm^{-1} in urea correspond to the C = O and -NH groups, respectively. Upon the formation of NADES-2, these peaks shifted to 1660 and 1605 cm^{-1}, respectively, providing evidence of hydrogen bonding between ChCl and urea. In the case of NADES-3 (Fig. 2c), the -OH and C = O peaks of malic acid shifted from 2873 and 1691 cm^{-1} to 2915 and 1722 cm^{-1}, respectively. Regarding NADES-4 (Fig. 2d), the C = O peak of betaine and the -OH and C-O peaks of glycerol shifted from 1612, 3288, and 1029 cm^{-1} to 1624, 3300, and 1038 cm^{-1}, respectively. Finally, for NADES-5 (Fig. 2e), the COO- peak of L-carnitine and the C-O peak of glycerol shifted from 1373 and 1029 cm^{-1} to 1391 and 1039 cm^{-1}, respectively. Collectively, the observed shifts in these characteristic peaks across all five NADESs confirm the formation of hydrogen bond interactions between the respective HBA and HBD components, thereby validating the successful synthesis of the targeted NADESs.

Figure S1 presents the H-NMR spectra of the five synthesized NADESs alongside their individual components. In H-NMR spectroscopy, the formation of hydrogen bonds induces a deshielding effect on the active hydrogen atoms, resulting in a distinct downfield shift (i.e., a shift to a higher chemical shift value) in their resonance signals [28]. As observed in Figure S1, the active hydrogen signals of the HBDs in all NADESs exhibit significant downfield shifts attributed to hydrogen bond formation with the HBAs. The specific chemical shift values are summarized in Table S2. Complementing the spectral analysis, the interaction energies (ΔE) of the five NADESs were determined using quantum mechanical calculations. As detailed in Table 1 and Figure S2, the calculated ΔE values are −22.45, −22.95, −24.04, −23.24, and −25.71 kcal mol^{-1}, respectively. It is noteworthy that these interaction energies were calculated based on a simplified 1:1 molar ratio model. Although the experimental NADESs were prepared at a 1:2 ratio (due to the fact that a 1:2 ratio typically has a lower melting point, it is more suitable for the lubrication field), the calculated trends effectively represent the relative strength of the intermolecular interactions. Consequently, when ChCl serves as the HBA, the hydrogen bond strength follows the sequence: NADES-3 > NADES-2 > NADES-1. When glycerol acts as the HBD, the strength follows the order: NADES-5 > NADES-4 > NADES-1. These results align well with the shifts observed in the ^{1}H-NMR spectra.

The melting temperature and decomposition temperature are key characteristics that define the temperature range within which NADESs remain in a liquid state [29].

Table 1. Physicochemical properties of NADESs.

Sample	Interaction energies ΔE (kcal mol)	Melting temperature (°C)	Decomposition temperature (°C)	Viscosity (Pa·s)	Contact angle on 45# steel (°)
NADES-1	22.45	−77.6	263.4	0.390	85.2 ± 0.5
NADES-2	22.95	21.8	242.3	0.591	80.4 ± 0.3
NADES-3	24.04	−37.3	241.5	54.785	45.2 ± 0.6
NADES-4	23.24	−71.1	266.2	1.584	71.4 ± 1.6
NADES-5	25.71	−55.6	200.7	9.525	69.9 ± 0.6

The melting temperatures of the five NADESs were determined via DSC. As summarized in Table 1 and Figure S3, the melting temperatures of NADES-1, NADES-2, NADES-3, NADES-4, and NADES-5 are −77.6°C, 21.8°C, −37.3°C, −71.1°C, and −55.6°C, respectively. In contrast to the melting temperatures of the individual precursors (glycerol: 17.8°C, ChCl: 302°C, urea: 133°C, malic acid: 101°C, betaine: 293°C, and L-carnitine: 200°C), the synthesized NADESs exhibit a significant depression in melting point, which is a defining characteristic of deep eutectic systems. Furthermore, the thermal stability of the five NADESs was evaluated using thermogravimetric (TG) and differential thermogravimetric (DTG) analyses. The TG and corresponding DTG curves are presented in Figure S4. The results indicate that all five NADESs exhibit an onset decomposition temperature above 200°C, with complete decomposition occurring at approximately 300°C. Evidently, they all possess excellent thermal stability, ensuring reliable performance under relatively high-temperature conditions. Collectively, the above results demonstrate that the prepared NADESs have a wide range of liquid operating temperatures.

Viscosity quantifies the internal flow resistance of a fluid and determines its ability to form a lubricating film, making it a fundamental performance indicator for lubricating oils [30]. The dynamic viscosities of the five NADESs were measured using a rheometer. As illustrated in Figure S5a and Table 1, at a shear rate of $100\,\mathrm{s}^{-1}$, the measured viscosities are 0.390, 0.591, 54.785, 1.584, and 9.525 Pa·s, respectively. It is noteworthy that, for the five NADESs, the hydrogen-bonding strength exhibits a positive correlation with viscosity; that is, stronger hydrogen bonding corresponds to higher dynamic viscosity. In addition, we also measured the viscosity of commercial lubricating oil PAO40, which was 0.775 Pa·s.

The affinity of lubricants to sample surfaces is evaluated by their wettability [31]. To assess this, the contact angles of the five NADESs on 45# steel were measured at 20°C, as illustrated in Figure S5b and Table 1. The results indicate that the contact angles of NADES-1, NADES-2, NADES-3, NADES-4, NADES-5, and PAO40 are 85.2°, 80.4°, 45.2°, 71.4°, 69.9°, and 30.2°, respectively. Notably, there is no direct correlation between contact angle and viscosity for these NADESs. Among NADES-1, NADES-2, and NADES-3, NADES-3 exhibited the smallest contact angle. As shown in the electrostatic potential map in Figure S6, red regions denote positive potential, while blue regions denote negative potential. The smaller contact angle of NADES-3 is likely attributed to the strong electronegativity of the carboxyl group, which facilitates coordination bonding with the metal surface. Comparing NADES-1 and NADES-2, it is evident that NADES-2 displays a smaller contact angle despite the lower electronegativity of urea compared to glycerol. This suggests that the amino group in urea possesses a stronger tendency to form coordination complexes with metals, thereby further reducing the contact angle. Regarding NADES-1, NADES-4, and NADES-5, the contact angle follows the descending order: NADES-1 > NADES-4 > NADES-5. This trend aligns with the higher electronegativity of L-carnitine compared to betaine and betaine's higher electronegativity than ChCl. Moreover, the chloride ions in ChCl may be encapsulated by glycerol, limiting their interaction with the metal surface, resulting in a relatively large contact angle for NADES-1. Consequently, both the electronegativity of the NADES components and their coordination affinity with metals play a crucial role in governing the contact angle.

3.2 Corrosion behavior and chemical stability

To evaluate the corrosion behavior of the prepared NADESs, the 45# steel used in this experiment was subjected to static immersion tests. The polished and cleaned steel specimens were fully submerged in the NADESs at room temperature (20°C) for a duration of 7 days, during which optical images were captured daily to monitor surface changes. Figure S7 illustrates the surface evolution of the 45# steel throughout the 1-to-7-day immersion period. It can be observed that the specimens immersed in the NADESs exhibited no visible corrosion pits. Even after 7 days of immersion, the surfaces showed no significant degradation and retained their original metallic luster. These immersion tests demonstrate that the synthesized NADESs possess excellent non-corrosive properties. Furthermore, comparative FTIR analysis of the NADESs before and after friction was conducted. As depicted in Figure S8, the results indicate that the chemical components of the NADESs remained unchanged after the friction process, confirming their high chemical stability.

3.3 Tribological performance analysis

To systematically investigate the tribological properties of NADESs with varying hydrogen bond strengths, the five synthesized NADESs were categorized into two groups (see

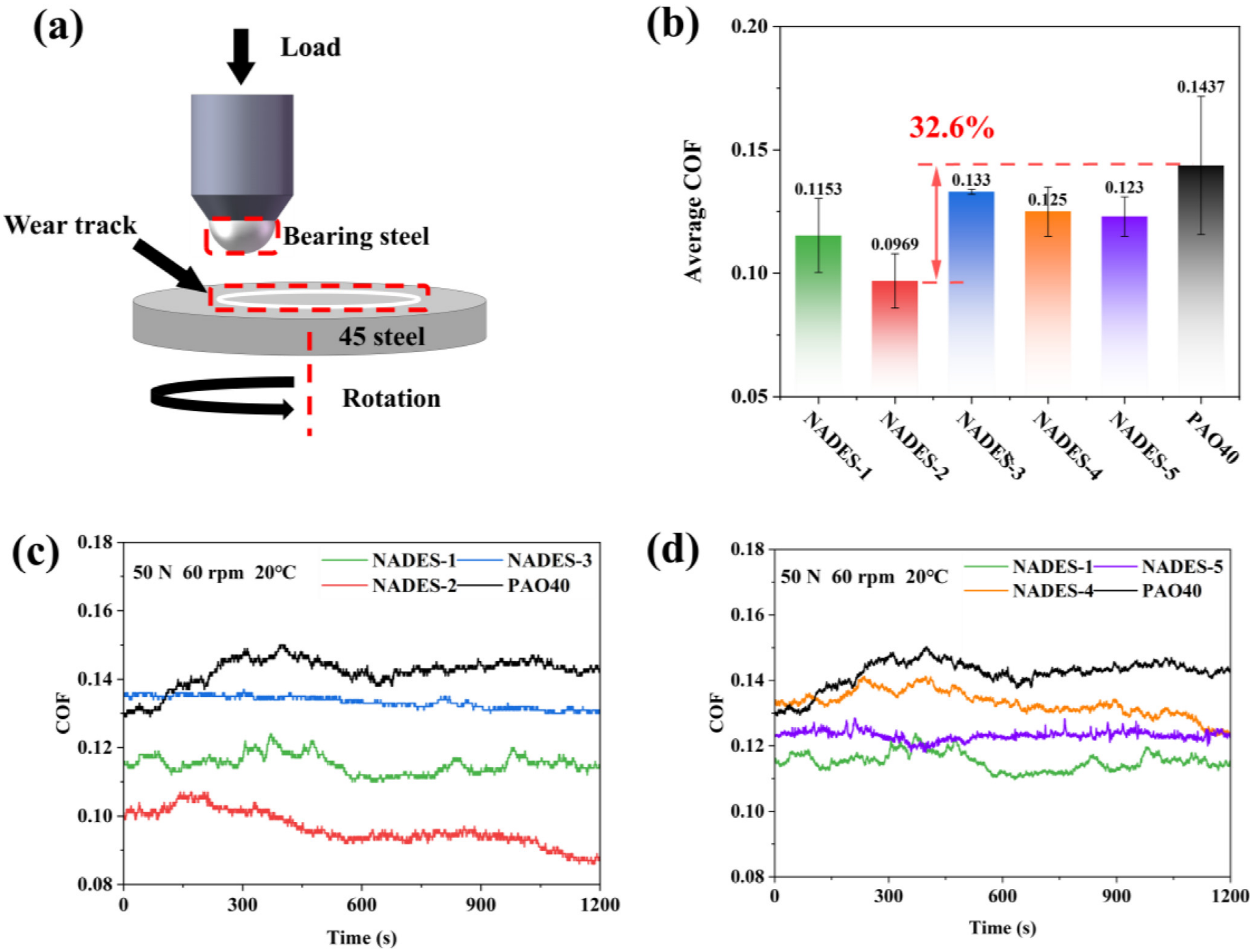

Fig. 3. (a) Schematic diagram of the tribological test configuration; (b) average COF for different lubricants; and (c, d) friction coefficient curves under 50 N and 60 rpm.

Tab. S1) based on variations in HBDs and HBAs. The first group comprises NADES-1, NADES-2, and NADES-3, which share an identical HBA but differ in their HBDs constituents. The second group consists of NADES-1, NADES-4, and NADES-5, characterized by the same HBD but distinct HBAs. Figure 3a presents a schematic diagram of the friction experiments using the GCr15-45# steel contact pair.

As illustrated in Figures 3b and 3c, when ChCl serves as the HBA, the friction coefficient of NADES-1 exhibits marked fluctuations characterized by numerous peaks and valleys, yielding an average friction coefficient of 0.1153. This indicates that NADES-1 exhibits poor lubrication stability throughout the friction process. In contrast, NADES-2 displays a smoother profile with minimal fluctuations. Instead of erratic peaks, it shows a stable decreasing trend, with an average friction coefficient of 0.0969. This enhancement of this stability is attributed to the higher hydrogen bond strength in NADES-2, which stabilizes the hydrogen-bonding network, making it less prone to disruption and limiting molecular mobility. Furthermore, as shown in Table 1, the amino groups in urea can form coordination bonds with metals, which strengthens the affinity of NADES-2 for metal surfaces and thereby reduces friction. Although NADES-3 possesses the strongest hydrogen bonding interactions and contains carboxyl groups capable of strong coordination with metals, theoretically suggesting a lower friction coefficient due to improved wettability, the experimental results are contrary to this expectation. Specifically, the friction coefficient of NADES-3 is higher than those of NADES-1 and NADES-2, with an average of 0.1333. This phenomenon is attributed to the excessively high viscosity of NADES-3, which impedes mass transfer and hinders the rapid recombination of hydrogen bonds, resulting in higher friction. The infrared characterization in Figure S8 verifies that the chemical composition of NADES-3 remains unchanged. Despite its high friction coefficient, NADES-3 demonstrates superior stability, evidenced by an almost linear friction curve. This is likely due to its high viscosity and strong intermolecular hydrogen bonding interactions, which maintain a stable equilibrium state even under shear stress. Consequently, it can be inferred that stronger hydrogen bonding interactions significantly enhance the lubrication stability of NADESs.

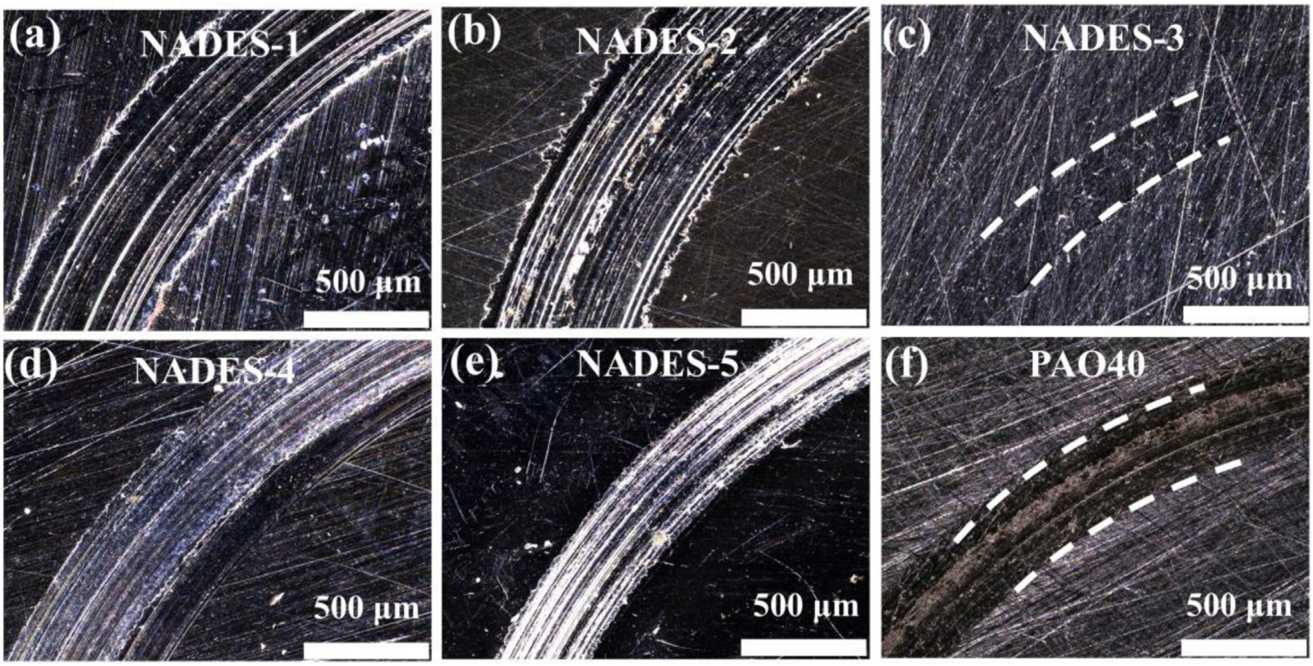

Fig. 4. Optical micrograph of wear tracks under 50 N and 60 rpm. (a) NADES-1; (b) NADES-2; (c) NADES-3; (d) NADES-4; (e) NADES-5; (f) PAO40.

Regarding the second group of NADESs, no significant difference in the COF was observed among the three samples, as shown in Figure 3d. However, the fluctuation of NADES-1 remains the most pronounced, while NADES-4 exhibits good stability with an average friction coefficient of 0.125. NADES-5 demonstrates superior stability throughout the entire friction process, with an average friction coefficient of 0.123. Notably, as the hydrogen bond strength increases (Fig. S2), the stability of NADESs is enhanced. Moreover, compared with ChCl in NADES-1, betaine in NADES-4 and L-carnitine in NADES-5 restrict molecular mobility more effectively after forming hydrogen bonds with glycerol. Conversely, the chloride ions in ChCl exhibit relatively high mobility, which accounts for the superior stability of NADES-4 and NADES-5. Additionally, commercial lubricant PAO40 was selected as a benchmark. As shown in Figure 3, the average friction coefficient of PAO40 is 0.1437, which is significantly higher than those of the NADESs. Specifically, NADES-2 exhibits the lowest friction coefficient, representing a 32.6% reduction compared to PAO40, thereby highlighting its excellent lubrication performance.

Figure 4 displays the optical micrographs of the wear tracks. Attributed to its strong hydrogen-bond interactions, high viscosity, and strong affinity for the metal surface, NADES-3 exhibits a well-defined boundary post-wear, with an extremely faint wear track, signifying minimal wear. In the second group of NADESs, a clear trend is observed: as the hydrogen-bond strength increases, the boundaries of the wear tracks become increasingly defined, smooth, and uniform. Among these, NADES-5 displays the most regular and distinct boundary, exhibiting the most uniform wear while retaining its metallic luster. This phenomenon is ascribed to the strong hydrogen-bond strength of NADES-5, which restricts molecular mobility, facilitating the formation of a stable and robust molecular adsorption film that reduces wear. Conversely, PAO40, due to its nonpolar nature, fails to form an effective protective tribofilm. Its wear track is characterized by a rough and indistinct boundary, with severe, uneven wear.

Wear volume serves as a critical metric for evaluating lubrication performance. Figure 5a presents the 3D topography images of the wear tracks, from which the wear width and depth were extracted. As illustrated in Figures 5b and 5c, within the first group, NADES-2 exhibits the most pronounced wear dimensions (yielding a wear width of 440 μm and a depth of 6.3 μm). This is likely attributed to the presence of urea in NADES-2, which may destabilize the protective iron oxide layer, thereby exacerbating wear. In contrast, NADES-3 demonstrates the minimal wear dimensions, with a width of merely 218 μm and a depth of 1.2 μm. This superior performance is ascribed to its strong hydrogen-bond strength, where the carboxyl group facilitates robust coordination and tribochemical reactions with iron, forming a protective iron carboxylate layer that effectively mitigates wear under load. Regarding the second group of NADESs, a comparison reveals that NADES-1, characterized by weaker hydrogen bonding, suffers the most severe wear. As the hydrogen-bond strength increases, the wear dimensions exhibit a corresponding decrease. Furthermore, the molecular structure of HBAs plays a pivotal role in wear morphology: longer chains, such as those in L-carnitine, impart elastic compressibility, thereby reducing wear depth. The carboxyl groups in both betaine and L-carnitine are capable of forming coordination bonds with the metal, contributing to the reduction of wear track dimensions. In comparison to the NADESs, the commercial lubricant

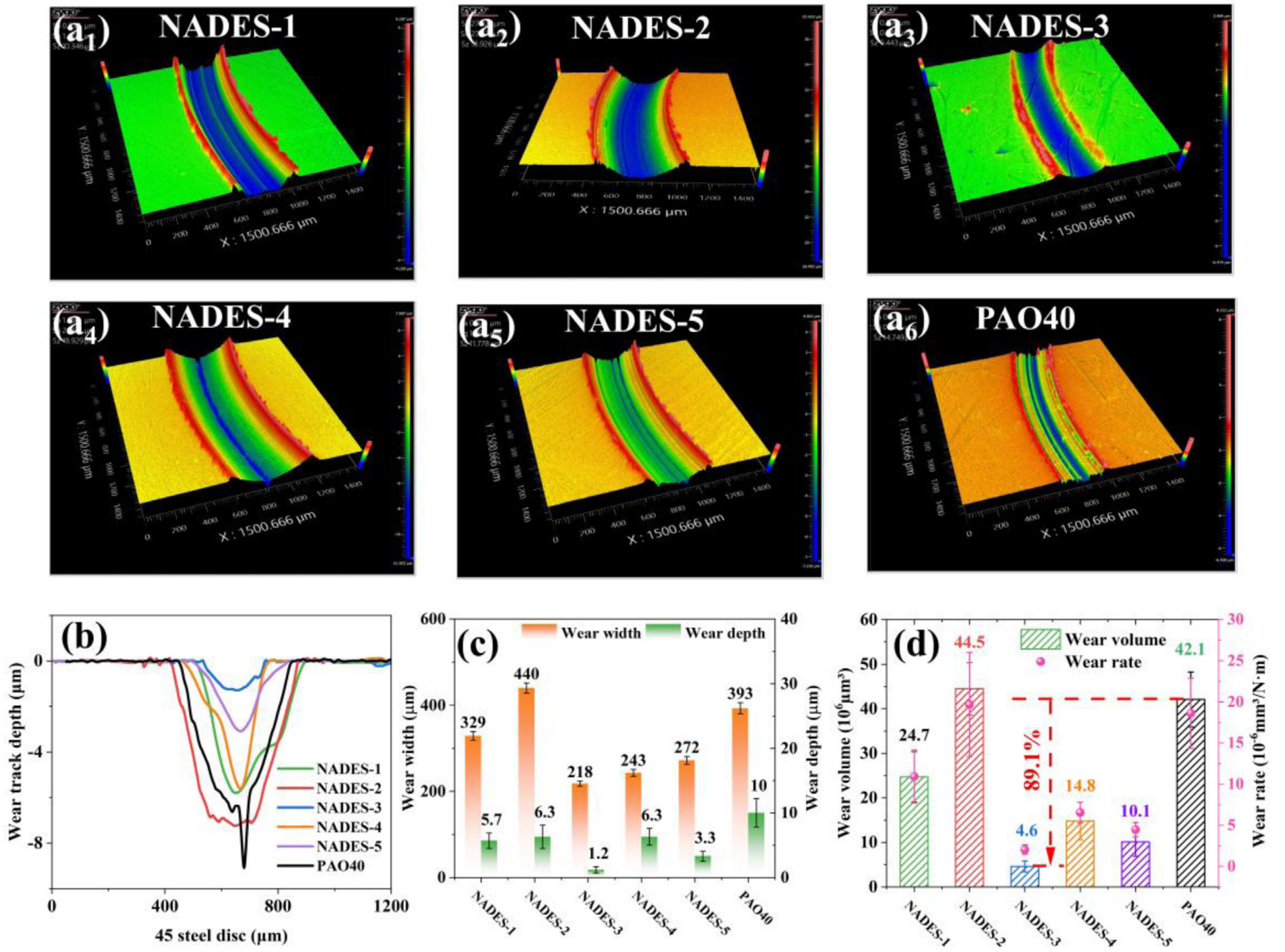

Fig. 5. (a) 3D morphologies of wear tracks; (b) cross-sectional profiles; (c) wear track dimensions (width and depth); and (d) wear volume and wear rate of NADESs and PAO40 under 50 N and 60 rpm.

PAO40 exhibits a substantially higher wear depth of 10.0 µm, representing an 88% increase compared to NADES-2, underscoring the inferior anti-wear performance of PAO40.

Figure 5d quantifies the wear volume of the wear tracks. Relative to PAO40, the wear volumes lubricated by NADES-1, NADES-3, NADES-4, and NADES-5 decreased by 41.3%, 89.1%, 64.8%, and 76.2%, respectively, highlighting the significant anti-wear capabilities of these NADESs. However, NADES-2 damages the protective layer of iron oxide, resulting in relatively severe wear comparable to that of PAO40. The observed wear reduction is governed by the interactions between polar functional groups (such as hydroxyl (R-OH) and amino (R-NH) groups) within the NADESs and the metal surfaces. According to the model proposed by Hardy and Doubleday [32], polar molecules adsorb onto the surface to form a closely packed, vertically oriented monolayer. In contrast, PAO40 lacks these polar functional groups, preventing the formation of such protective films, which results in a significantly larger wear volume compared to the NADESs.

To investigate the load-bearing capacity of NADESs, their friction performance was further evaluated under loads of 100 and 150 N. Figures 6a and 6b illustrate the friction coefficient of NADESs at 100 N. Upon increasing the load to 100 N, the friction coefficient of the NADESs remains virtually unchanged compared to the values obtained under 50 N. As shown in Figure 6a, the average friction coefficients of NADES-1 and NADES-2 are 0.1150 and 0.1094, respectively, exhibiting significant fluctuations. However, attributed to the enhanced hydrogen bonding, the friction coefficient curve of NADES-3 shows stability consistent with the 50 N condition, with an average friction coefficient of 0.1350. Figure 6b presents the friction coefficient of the second group of NADESs under 100 N, with average friction coefficients of 0.1201 and 0.1257 for NADES-4 and NADES-5, respectively. The friction coefficient curve of NADES-5 is also a straight line with almost no fluctuations, whereas NADES-4 and NADES-1 exhibit significant fluctuations. The fluctuation of the commercial lubricating oil PAO40 is the most pronounced, with an average friction coefficient of 0.1335, indicating that the lubrication stability of PAO40 is significantly inferior to that of the NADESs. As shown in Figures 6c and 6d, even when the load increases to 150 N, the average friction coefficient of the NADESs remains stable and largely unchanged. The friction curves of

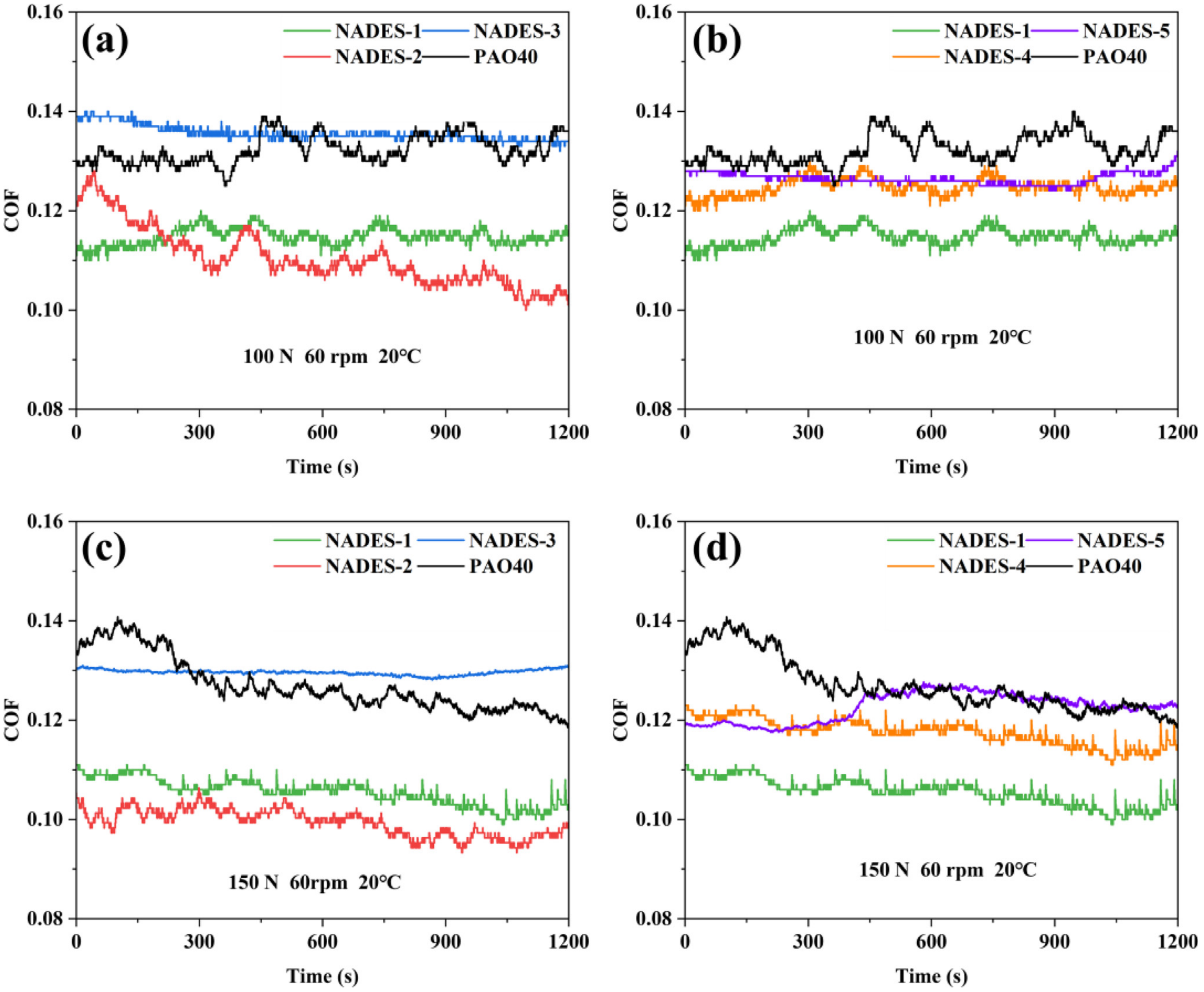

Fig. 6. Friction coefficient curves of NADESs and PAO40 under high-load conditions: (a, b) 100 N and (c, d) 150 N.

NADES-3 and NADES-5 maintain stability due to their high hydrogen bond strength, with average friction coefficients of 0.1301 and 0.1233, respectively. In contrast, the friction curve of NADES-1 shows multiple abrupt spikes, with an average friction coefficient of 0.1050. This may be attributed to its weak hydrogen bond strength and insufficient load-bearing capacity, resulting in the continuous breaking and reforming of hydrogen bonds under stress. NADES-2 exhibits the lowest friction coefficient at 0.0984. The average friction coefficient of NADES-4 is slightly lower than that of NADES-5 at 0.1200. Commercial lubricants exhibit the poorest lubrication performance, with an average friction coefficient of 0.1280.

As illustrated in Figure 7, upon increasing the load, the friction coefficient of the NADESs remained nearly stable at higher loads (100 and 150 N). While the load-dependent pattern of the COF may not be typical, this phenomenon has been observed in numerous studies on both dry and lubricated sliding contacts of various bulk materials [33]. In conclusion, the friction coefficients of the tested NADESs

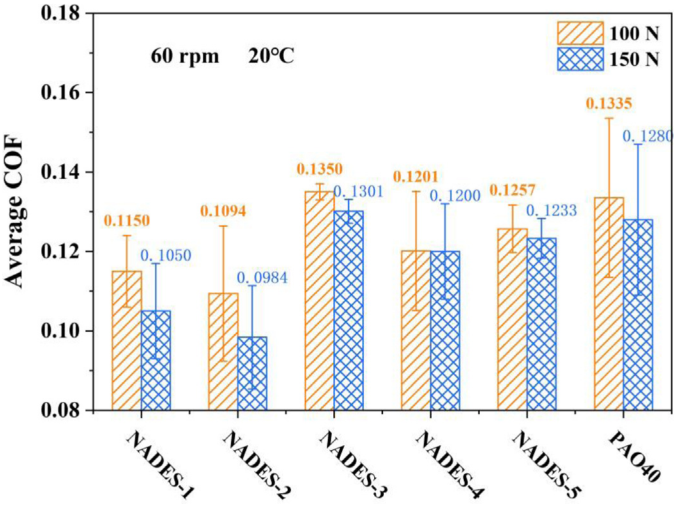

Fig. 7. The average COF of NADESs and PAO40 under loads of 100 and 150 N at 60 rpm.

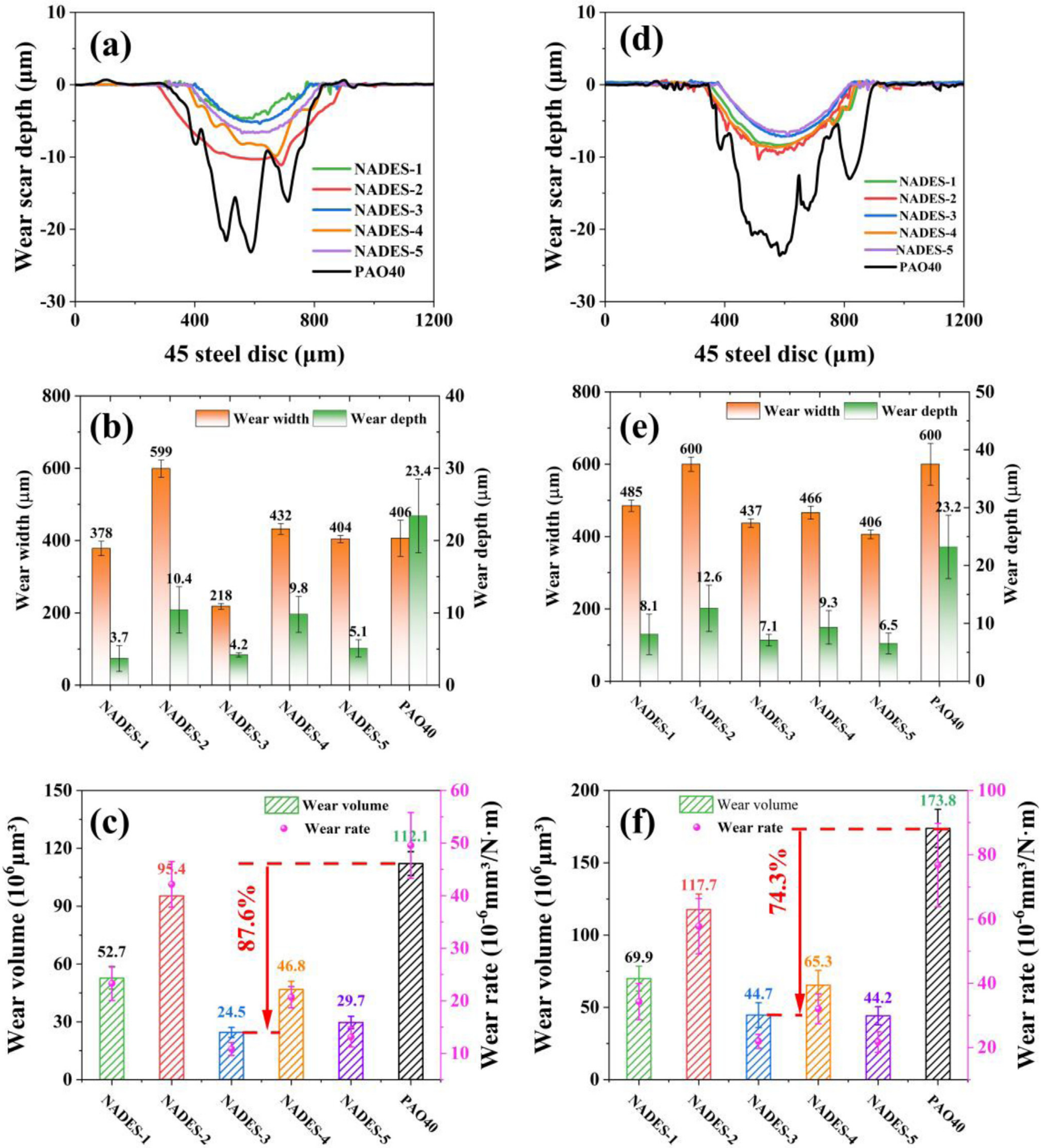

Fig. 8. Wear characterization of NADESs and PAO40 under high loads: (a–c) 100 N and (d–f) 150 N. (a, d) Cross-sectional profiles of wear tracks; (b, e) wear track dimensions (width and depth); and (c, f) wear volume and wear rate.

remained relatively stable throughout the entire test process and did not exhibit any abrupt surges, indicating that these NADESs possess excellent load-bearing capacity.

Figure 8 presents a comparison of the wear dimensions and wear volume for the NADESs and PAO40 under loads of 100 and 150 N. The corresponding optical micrographs and 3D morphologies are displayed in Figures S9 and S10. Regarding the second group of NADESs, the long chains in L-carnitine provide elastic compressibility, resulting in the shallowest wear depth. In comparison to PAO40, the depth of wear tracks lubricated by NADESs decreased significantly. This phenomenon is attributed to the formation of an adsorbed lubricating film by the polar molecules in NADESs, which effectively mitigates vertical wear.

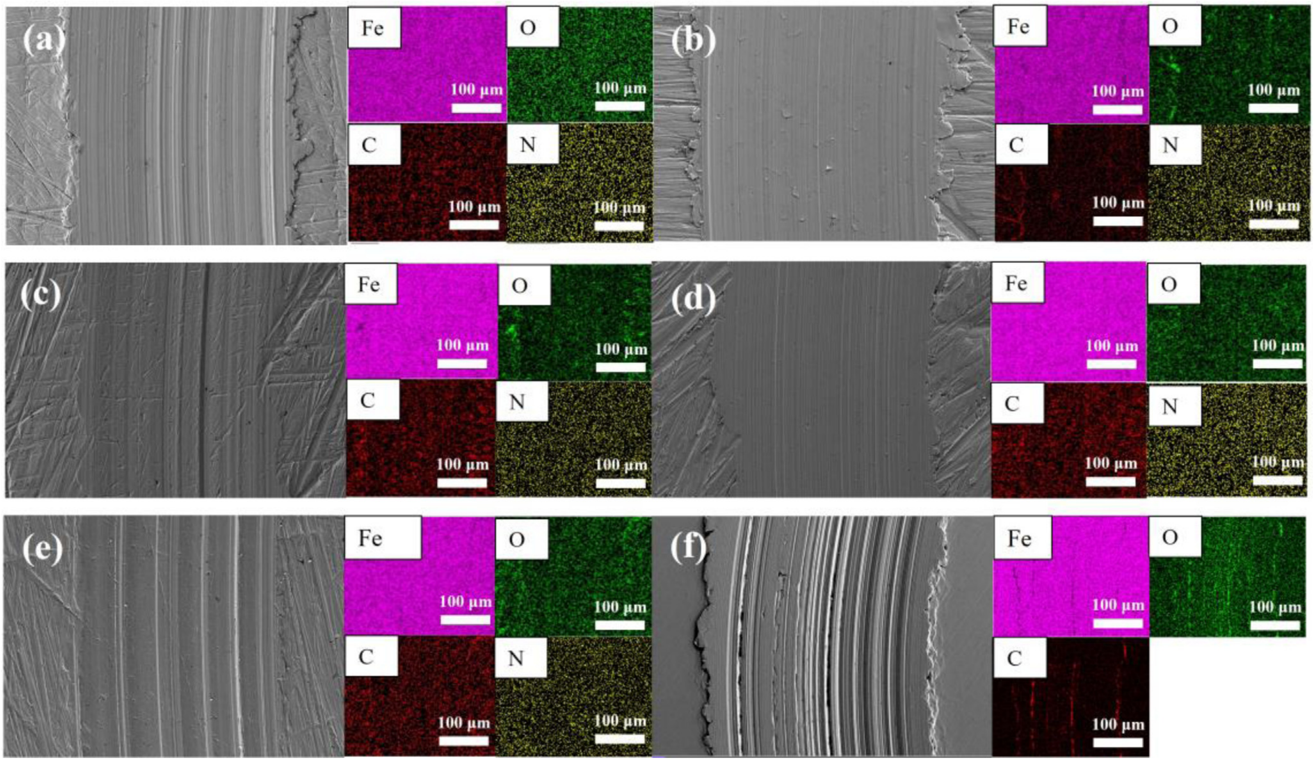

Fig. 9. EDS images of scratches on the surface of 45 steel under a load of 50 N. (a) NADES-1; (b) NADES-2; (c) NADES-3; (d) NADES-4; (e) NADES-5; and (f) PAO40.

In contrast to the friction coefficient trends, the wear volume of NADESs increases with increasing load, aligning with the predictions of the classical Archard wear law. Relative to the commercial lubricant PAO40, NADESs exhibit superior wear resistance, with NADES-3 demonstrating the optimal performance. Specifically, the wear volumes of NADES-3 under loads of 100 and 150 N were 24.5×10^6 and 44.7×10^6 μm^3, respectively, representing reductions of 87.6% and 74.3% compared to PAO40.

3.4 Analysis of wear surface and lubricating mechanism

To gain a deeper understanding of the lubrication mechanism of NADESs, the surface composition and chemical states of the wear tracks were analyzed by EDS and XPS. Prior to the characterization, the samples were cleaned with ethanol and dried. The 45# steel disc substrate, primarily composed of Fe, C, O, Cr, Si, and Mn, served as the friction pair. Figure 9 presents the scanning electron microscopy images. The wear surface lubricated with PAO40 exhibits severe abrasive wear, characterized by deep abrasive grooves and rough, ill-defined boundaries. In contrast, the wear track surface lubricated by NADESs is smooth and flat, featuring distinct wear boundaries and significantly reduced wear, indicating superior lubrication performance. To elucidate the lubrication mechanism, elemental mapping of the wear tracks was performed. The *N* element derived from the NADESs was detected on the worn surface, indicating the formation of a protective adsorption film, while PAO40 failed to form such a layer. These findings elucidate why NADESs exhibit superior lubrication performance compared to the commercial lubricant PAO40.

As shown in Table S3, compared to the pristine substrate, an increase in both O and C content was detected on the worn surfaces lubricated with NADESs. This suggests that the NADESs adsorb onto the steel surface or form iron oxides and hydroxides via tribochemical interactions with the substrate. The increase in oxygen content is most pronounced in NADES-2. This phenomenon is likely attributed to urea destabilizing the protective oxide layer, thereby exposing nascent metal surfaces that subsequently react with ambient oxygen and moisture to form substantial iron oxides.

To further investigate the chemical composition of the tribofilm, XPS analysis was performed. Figure 10 presents the XPS spectra of the worn surfaces after lubrication with NADESs. Given the superior lubrication performance of NADES-2 (as evidenced by its low friction coefficient), we focused on analyzing the high-resolution XPS spectra of C1s, O1s, Fe2p, and N1s for the surface lubricated by this solvent. In Figure 10a, the C1s spectrum of the worn surface contains four peaks located at 283.33, 284.80, 286.66, and 288.63 eV, corresponding to C-Si, C-C/C-H, C-OH, and O-C = O groups [34–37], respectively. As shown in Figure 10b, the O1s peaks at 530.04, 531.76, and 533.70 eV are assigned to iron oxides, -OH, and O = C-O/-C-O- [38–43]. The presence of C-O and C = O bonds suggests the occurrence of tribochemical oxidation. Furthermore, this indicates that the hydroxyl groups in ChCl can adsorb onto metal surfaces through polar interactions, forming Fe-O

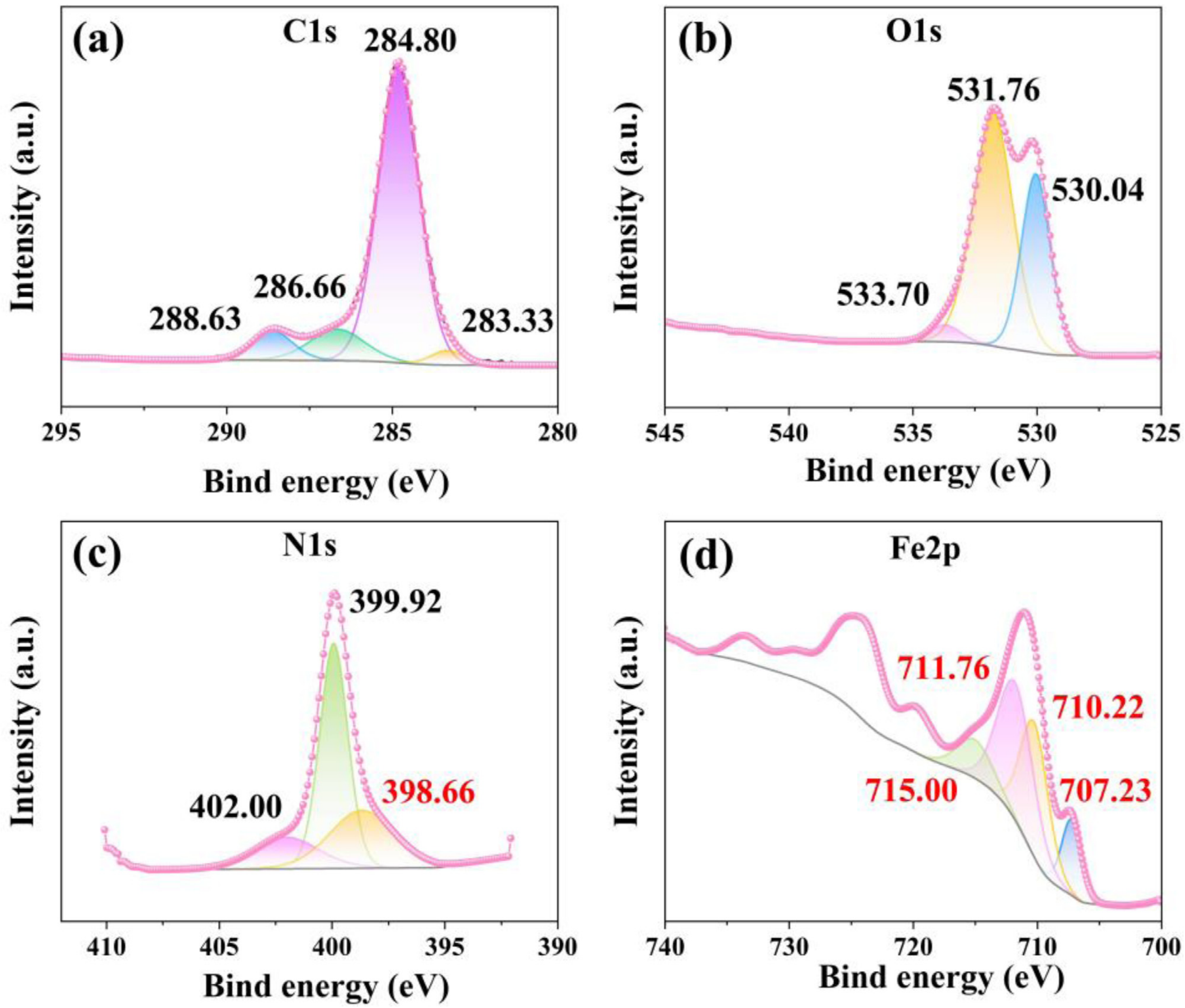

Fig. 10. XPS spectra of worn surfaces (a) C1s, (b) O1s, (c) N1s, and (d) Fe2p under the action of NADES-2.

linkages. Regarding the Fe2p spectrum in Figure 10d, the binding energy peaks near 707.23, 710.22, 711.76, and 715.00 eV are attributed to Fe/Fe_3O_4, $FeCl_3$/Fe_3O_4/Fe_2O_3, FeOOH, Fe^{2+}/FeO, and $FeCl_3$ [44–46], respectively. According to Figure 10c, the N1s spectrum exhibits peaks at approximately 398.66, 399.65, and 402.00 eV, corresponding to -NH_2, C-N-C [47], and N-O. These peaks are attributed to metal nitrides, indicating that ChCl–urea NADES participates in frictional chemical reactions.

The high-resolution spectra of C, O, N, and Fe suggest that the amino group in NADES-2 undergoes chemisorption on the worn surface, facilitating the formation of iron oxides, hydroxides, and nitrides during the sliding process. The oxygen and moisture in the air also facilitate the formation of this chemical reaction layer. Consequently, we propose that the tribofilm of NADES-2 is structurally composed of two distinct layers: an adsorption layer formed by polar molecules (providing high vertical load capacity and low shear strength) and a tribochemical reaction layer consisting of iron oxides and hydroxides. The synergistic effect of these layers contributes to the superior lubricity of NADES-2 compared to other samples. As shown in Figure S11, the characteristic peaks of C1s, O1s, and Fe2p in the spectra of the other NADESs are comparable, indicating that their primary tribochemical products also consist of iron oxides and iron hydroxides.

Based on the tribological results and surface characterization, a lubrication mechanism for the studied NADESs is proposed. As illustrated in Figure 11, the tribofilm formed by NADESs consists of two distinct layers. The inner layer is a tribochemical film composed of iron oxides and hydroxides, while the outer layer is a polar molecule adsorption film formed by the polar groups of NADESs (e.g., hydroxyl groups and amino groups). The excellent friction-reducing performance of NADESs is attributed to the adsorption of these polar molecules, which form a monolayer characterized by high vertical rigidity and low shear strength at the contact interface. Analysis of the wear track morphologies and wear volume data reveals that hydrogen bond strength influences the integrity of the

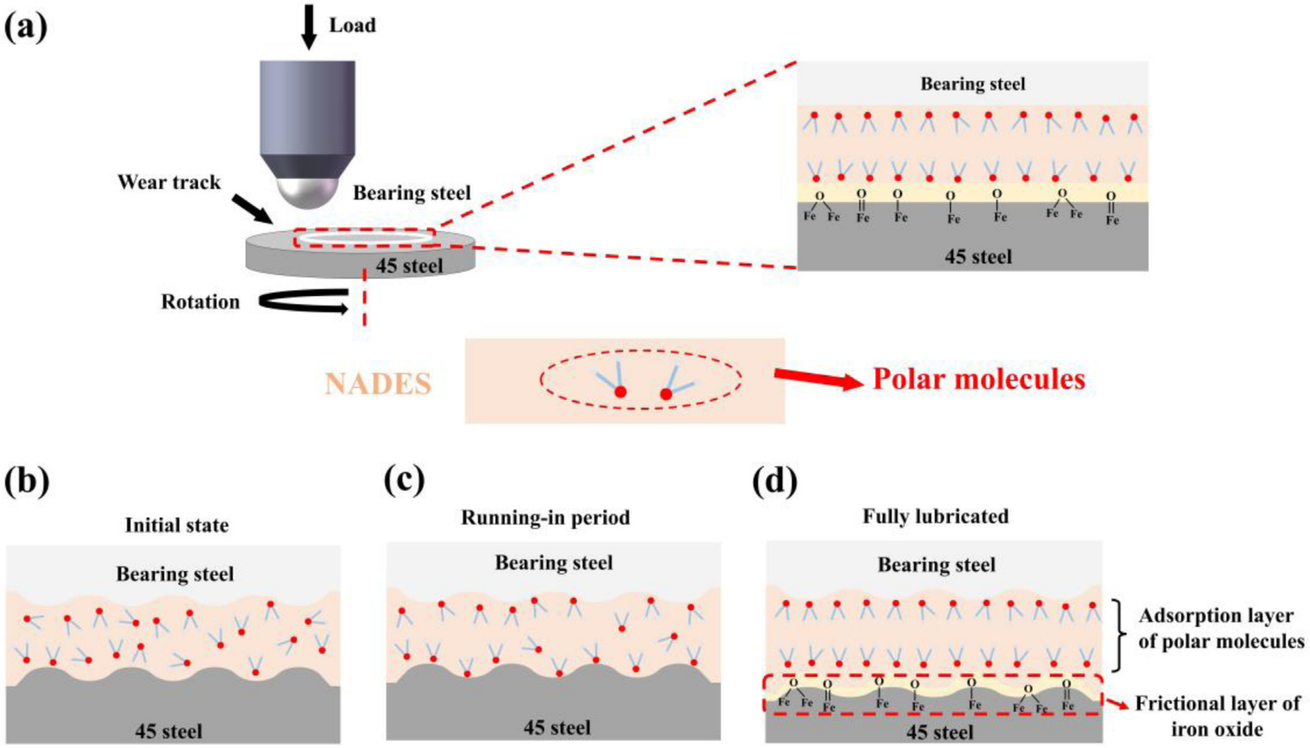

Fig. 11. Illustration of the lubrication mechanism model: (a) Schematic of molecular adsorption at the contact zone; and (b–d) Stages of film formation ranging from the initial state to the fully lubricated regime.

polar adsorption layer. Higher hydrogen bond strength restricts molecular mobility within the system, resulting in enhanced rigidity of the adsorption layer and, consequently, superior anti-wear performance. In contrast to PAO40, this polar adsorption layer plays a pivotal role in mitigating wear. Furthermore, during the sliding process, ambient oxygen and moisture, in conjunction with hydroxides and oxides, contribute to the formation of a tribochemical film, thereby further reducing friction and wear.

3.5 Experimental analysis of friction torque of ball screw

The contact kinematics between the ball and nut in a ball screw pair are analogous to the configuration of the friction and wear experiments. Specifically, the sliding contact of the ball against the disc in the tribometer mimics the interaction between the rolling elements and the nut raceway. Therefore, measuring the friction torque of the ball screw pair serves to further validate the tribological behaviors observed in the fundamental friction and wear tests. To quantify the friction torque during operation, the dedicated measurement system illustrated in Figure 12 was employed.

The servo motor is equipped with a tip on the right side, which engages the shaft end of the ball screw pair to provide support. Rotation of the servo motor drives the synchronous rotation of the ball screw. The tip provides precise centering, ensuring that the rotation axis of the workpiece remains stable during friction torque measurement, thereby improving the accuracy of the measurement. The opposite end of the ball screw is supported by the tailstock center and secured with a locking device. The measuring platform features a height-adjustable support structure, which accommodates ball screw pairs of different dimensions. The top of the support structure is fitted with a semi-circular protrusion that engages with the screw raceway. Consequently, the rotation of the nut is constrained by the support structure, converting the motion into pure axial translation of the measuring carriage along the linear guide rail. Simultaneously, the workbench moves axially at the same speed as the nut. A bolt mounted on the nut's flange face contacts the force sensor. The force detected by the sensor represents the tangential resistance of the ball screw pair, and the friction torque is calculated as the product of this force and the moment arm (the distance between the bolt and the screw axis). The sensor is calibrated using standard weights.

It should be noted that during the friction torque measurement, the force sensor is mechanically coupled to the nut. Consequently, the obtained friction torque is only the torque applied through frictional force at the contact point between the ball and nut at a distance L from the nut axis. The torque measured in the experiment is independent of the moments between ball-to-ball and ball-to-screw shaft. Forward and reverse dynamic torque tests are conducted on a ball screw pair to obtain sets of forward and reverse friction torque values. The arithmetic mean of these two values is taken as a single experimental result. To minimize measurement uncertainty, the test is repeated three times at each rotational speed. The average of the three experimental results is then calculated as the mean

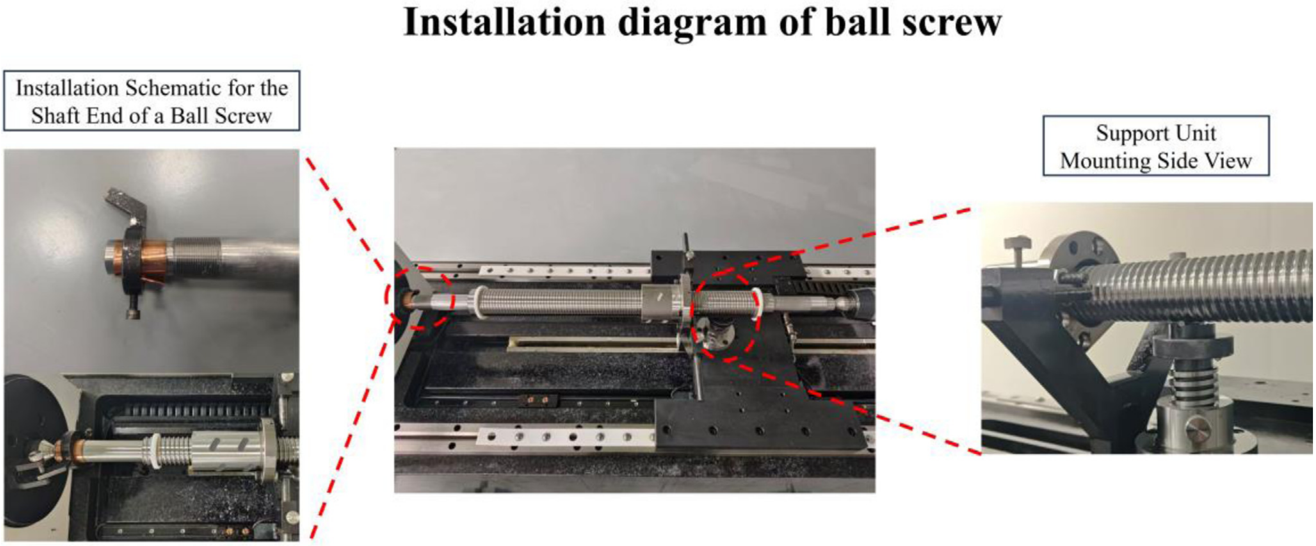

Fig. 12. Schematic diagram of ball screw installation.

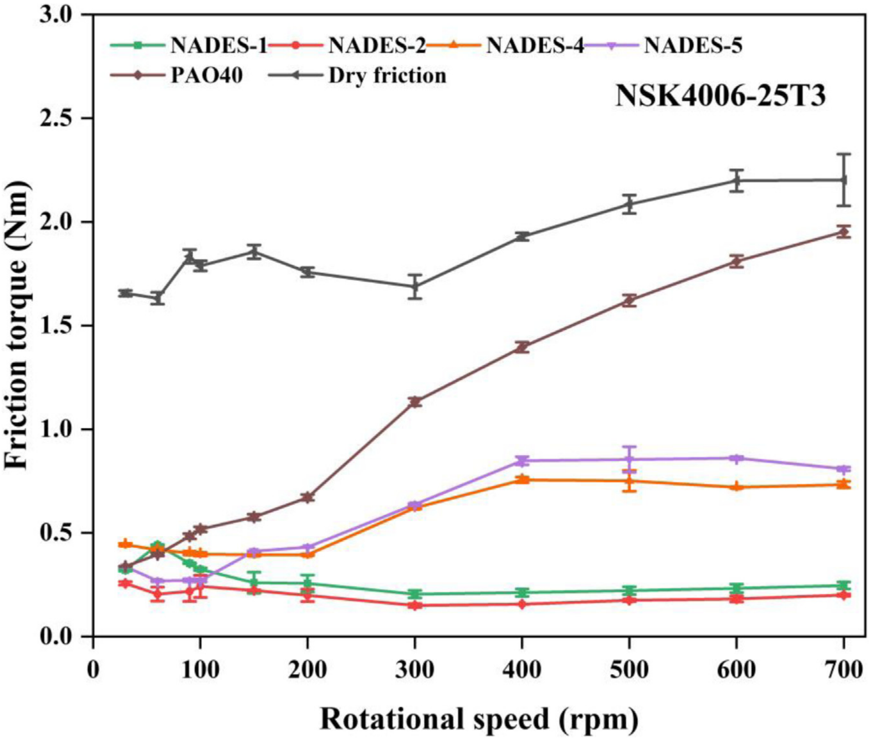

Fig. 13. Friction torque velocity relationship curve between nut and ball in ball screw under different lubrication conditions.

friction torque corresponding to that specific rotational speed. Additionally, due to the mild acidity of NADES-3, its lubrication performance on ball screw pairs was excluded from this investigation. The ambient temperature for the friction torque experiment is 20°C. When the speed reached 700 rpm, due to the set test stroke of 100 mm, the experimental time was relatively short, only about 5 s, and the temperature change response was slow. The temperature change inside the nut was not studied.

Figure 13 shows the variation of friction torque between the nut and ball of NSK4006-25T3 ball screw pair with rotational speed. Specifically, NADES-1 and NADES-2, the two lubricants with lower viscosity, exhibit relatively stable friction torque across the speed range, fluctuating between 0.2 and 0.4 Nm. Among them, NADES-2 demonstrates the superior lubrication performance, yielding a friction torque of 0.2 Nm at 700 rpm. NADES-1 exhibits a slightly higher friction torque of 0.2465 Nm at

700 rpm compared to NADES-2. Regarding the lubricants with high viscosity, the friction torques of NADES-4 and NADES-5 are 0.809 and 0.733 Nm, respectively. Notably, the friction torque of NADES-5 is lower than that of NADES-4, which is consistent with the findings from the tribometer tests. The lubrication performance of PAO40 is the poorest, with its friction torque increasing sharply with rotational speed. For instance, as the speed increases from 200 to 700 rpm, the friction torque surges from 0.671 to 1.953 Nm, indicating a significant degradation in lubrication efficacy, and the lubrication regime is unstable. At 700 rpm, it approaches a dry friction state, signifying a near-total loss of lubrication capability. This behavior contrasts sharply with that of the NADESs, suggesting that the lubricating film formed by PAO40 gradually ruptures as the speed increases. Even the NADES exhibiting the highest friction torque (NADES-4) represents a 58% reduction compared to PAO40, indicating a significant improvement in lubrication performance. Consistent with the lubrication mechanism analysis in Section 3.4, the polar groups (hydroxyl: R-OH and amino: R-NH_2) and ions in NADESs adsorb firmly onto the surfaces of balls and raceways through physicochemical adsorption, resisting desorption under shear forces. Consequently, NADESs maintain consistently low friction torque across the 30–700 rpm range, demonstrating superior lubrication performance compared to PAO40.

4 Conclusion

In this work, five representative NADESs with varying hydrogen bond strengths were developed to systematically investigate their lubrication mechanisms. The findings reveal that both hydrogen bond interactions and the molecular architecture of HBAs critically govern the tribological behavior of NADESs. Stronger hydrogen bonding restricts molecular mobility, facilitating the formation of a resilient lubricating film that reduces friction fluctuations and wear. Moreover, the structural features of HBAs, such as long alkyl chains and polar carboxyl groups, enhance coordination with metal surfaces, thereby significantly improving anti-wear capabilities. The friction torque tests of the ball screw pair further confirmed that compared with the commercial lubricant PAO40, the formulated NADESs reduce the friction torque between the ball and nut of the ball screw by at least 60% under high-speed conditions. This exceptional lubricity is ascribed to the formation of a reliable boundary film via physicochemical adsorption and tribochemical reactions, which ensures stability even under rigorous operating conditions. Collectively, this study not only elucidates the structure-property relationships in NADES lubrication but also provides theoretical guidance for designing next-generation, high-performance green lubricants for precision transmission systems.

Funding

This research was supported by The National Natural Science Foundation of China (grant No. 52075264).

Conflicts of interest

The authors declare that they have no known competing financial interests or personal relationships that could have appeared to influence the work reported in this paper.

Data availability statement

Data will be made available on request.

Author contribution statement

Lei Yuan: Writing original draft, Analysis, Data curation.
Zhaoyang Wang: Investigation, Methodology, Software.
Changguang Zhou: Supervision.
Michel Fillon: Validation.
Meng Wang: Resources.
Yibiao Wang: Conceptualization.
Wentao Bi: Writing review & editing.
Wenling Zhang: Visualization, Funding acquisition.
All authors read and approved the final manuscript.

Supplementary material

Fig. S1. Nuclear magnetic resonance hydrogen spectra of (a) NADES-1, (b) NADES-2, (c) NADES-3, (d) NADES-4, and (e) NADES-5.

Fig. S2. The stable configurations and the interaction energies ΔE of (a) NADES-1, (b) NADES-2, (c) NADES-3, (d) NADES-4, and (e) NADES-5.

Fig. S3. DSC curves of (a) NADES-1, (b) NADES-2, (c) NADES-3, (d) NADES-4, and (e) NADES-5.

Fig. S4. TG/DTG curves of (a) NADES-1, (b) NADES-2, (c) NADES-3, (d) NADES-4, and (e) NADES-5.

Fig. S5. (a) Dynamic viscosity curve and (b) contact angle of NADESs.

Fig. S6. Electrostatic potential maps of five NADESs.

Fig. S7. Photos showing the changes in the surface of 45# steel immersed in NADESs over time.

Fig. S8. FTIR spectra of the synthesized (a) NADES-1, (b) NADES-2, (c) NADES-3, (d) NADES-4, and (e) NADES-5 before and after the friction test.

Fig. S9. (a) Optical micrograph and (b) 3D morphology of wear tracks under 100 N.

Fig. S10. (a) Optical micrograph and (b) 3D morphology of wear tracks under 150 N.

Fig. S11. XPS spectra of worn surfaces with (a) NADES-1, (b) NADES-2, (c) NADES-3, (d) NADES-4, and (e) NADES-5.

Tab. S1. The DESs used in this study (molar ratio: 1:2).

Tab. S2. Chemical shifts (δ) and changes in chemical shifts ($\Delta\ \delta$) of HBAs, HBDs, and NADESs.

Tab. S3. Elemental content (%) of steel discs without wear and lubricated with NADESs.

The Supplementary Material is available at https://www.mechanics-industry.org/10.1051/meca/2026012/olm.

References

[1] J. Zhao, B. Qi, X. Song, H. Jiang, P. Dong, A modeling method for predicting friction torque of the preload double-nut ball screw based on thermal elastohydrodynamic lubrication, Int. J. Adv. Manuf. Technol. **124**, 4231–4251 (2023)

[2] X. Sui, J. Liu, G. Zhao, X. Wang, Y. Han, C. Gachot, $Ti_3C_2T_x$ MXene modified alkyl imidazolium ionic liquid-stearic acid composite materials as a potential lubricant for steel/steel contact, Wear **578**, 206151 (2025)

[3] D.K. Kiboi, J. Yan, E.C. Dillon, J.L. Viesca, M.G. Coleman, F. Mangolini, P. Iglesias, Physicochemical and lubricating properties of choline amino acid ionic liquids as neat lubricants for steel-steel contact, Wear **578**, 206198 (2025)

[4] X. Hou, H. Tang, L. Dai, X. Li, G. Lan, Z. Ai, Y. Jiang, C. Sheng, H. Wan, Potassium borate/graphene nanocomposite lubricant additive with anti-friction/wear and anti-corrosion functions for marine diesel engine burning low sulfur fuel, Wear **550**, 205395 (2024)

[5] S. Boyde, Green lubricants. Environmental benefits and impacts of lubrication, Green Chem. **4**, 293–307 (2002)

[6] D. Hörner, Recent trends in environmentally friendly lubricants, J. of Synth. Lubr. **18**, 327–347 (2002)

[7] G.C. Dugoni, M.E. Di Pietro, M. Ferro, F. Castiglione, S. Ruellan, T. Moufawad, L. Moura, M.F. Costa Gomes, S. Fourmentin, A. Mele, Effect of water on deep eutectic solvent/β-cyclodextrin systems, ACS Sustain. Chem. Eng. **7**, 7277–7285 (2019)

[8] D.V. Wagle, H. Zhao, G.A. Baker, Deep eutectic solvents: sustainable media for nanoscale and functional materials, Acc. Chem. Res. **47**, 2299–2308 (2014)

[9] K. Zhang, S. Ren, X. Yang, Y. Hou, W. Wu, Y. Bao, Efficient absorption of low-concentration SO_2 in simulated flue gas by functional deep eutectic solvents based on imidazole and its derivatives, Chem. Eng. J. **327**, 128–134 (2017)

[10] T. El Achkar, H. Greige-Gerges, S. Fourmentin, Basics and properties of deep eutectic solvents: a review, Environ. Chem. Lett. **19**, 3397–3408 (2021)

[11] K. Shahbaz, F.S. Mjalli, G. Vakili-Nezhaad, I.M. AlNashef, A. Asadov, M.M. Farid, Thermogravimetric measurement of deep eutectic solvents vapor pressure, J. Mol. Liq. **222**, 61–66 (2016)

[12] L.B. Santos, R.S. Assis, J.A. Barreto, M.A. Bezerra, C.G. Novaes, V.A. Lemos, Deep eutectic solvents in liquid-phase microextraction: contribution to green chemistry, TrAC Trends Anal. Chem. **146**, 116478 (2022)

[13] M. Jablonsky, A. Skulcová, A. Ház, J. Sima, V. Majová, Long-term isothermal stability of deep eutectic solvents, Bioresources **13**, 7545–7559 (2018)

[14] V.I. Vorobyova, O. Linyucheva, O.E. Chygyrynets, M. Skiba, G.S. Vasyliev, Comprehensive physicochemical evaluation of deep eutectic solvents: quantum-chemical calculations and electrochemical stability, Mol. Cryst. Liq. Cryst. **750**, 60–68 (2023)

[15] C. Yang, M. Gao, Q. Zhang, J. Zeng, X. Li, A.P. Abbott, In-situ activation of self-supported 3D hierarchically porous Ni3S2 films grown on nanoporous copper as excellent pH-universal electrocatalysts for hydrogen evolution reaction, Nano Energy **36**, 85–94 (2017)

[16] J. Zhang, Q. Kuang, Y. Jiang, Z. Xie, Engineering high-energy surfaces of noble metal nanocrystals with enhanced catalytic performances, Nano Today **11**, 661–677 (2016)

[17] G.P. Rachiero, P. Berton, J. Shamshina, Deep eutectic solvents: alternative solvents for biomass-based waste valorization, Molecules **27**, 19 (2022)

[18] H. Dou, M. Xu, L. Yang, B. Wang, A. Yu, L. Zhang, Z. Chen, Z. Jiang, Efficient ethylene/ethane separation by zwitterionic deep eutectic solvent membranes, J. Membr. Sci. **666**, 121181 (2023)

[19] S.D.A. Lawes, S.V. Hainsworth, P. Blake, K.S. Ryder, A.P. Abbott, Lubrication of steel/steel contacts by choline chloride ionic liquids, Tribol. Lett. **37**, 103–110 (2010)

[20] Y. Shi, L. Mu, X. Feng, X. Lu, Friction and wear behavior of CF/PTFE composites lubricated by choline chloride ionic liquids, Tribol. Lett. **49**, 413–420 (2013)

[21] J.E. Hallett, H.J. Hayler, S. Perkin, Nanolubrication in deep eutectic solvents, Phys. Chem. Chem. Phys. **22**, 20253–20264 (2020)

[22] Z. Li, E. Zhang, W. Li, H. Liu, Tribological study of two ammonium chloride-decanoic acid deep eutectic solvents (DESs) as high-performance lubricants, Friction **12**, 2441–2457 (2024)

[23] V. Jančíková, M. Jablonský, The future of green chemistry: evolution and recent trends in deep eutectic solvents research, Appl. Sci. **16**, 654 (2026)

[24] I. Juneidi, M. Hayyan, M. Hashim, Evaluation of toxicity and biodegradability for cholinium-based deep eutectic solvents, RSC Adv. **5**, 83636–83647 (2015)

[25] S.N. Steinmann, C. Corminboeuf, A system-dependent density-based dispersion correction, J. Chem. Theory Comput. **6**, 1990–2001 (2010)

[26] Y. Li, Y. Li, H. Li, X. Fan, H. Yan, M. Cai, X. Xu, M. Zhu, Insights into the tribological behavior of choline chloride—urea and choline chloride—thiourea deep eutectic solvents, Friction **11**, 76–92 (2023)

[27] K. Mulia, E. Krisanti, F. Terahadi, S. Putri. Selected natural deep eutectic solvents for the extraction of α-mangostin from mangosteen (Garcinia mangostana L.) Pericarpp, Int. J. Technol. **6**, 291–319 (2015)

[28] D. Cao, Q. Liu, W. Jing, H. Tian, H. Yan, W. Bi, Y. Jiang, D. D.Y Chen, Insight into the deep eutectic solvent 31 extraction mechanism of flavonoids from natural plant, ACS Sustain. Chem. Eng. **8**, 19169–19177 (2020)

[29] A. Khan, R. Singh, P. Gupta, K. Gupta, O.P Khatri, Aminoguanidine-based deep eutectic solvents as environmentally-friendly and high-performance lubricant additives, J. Mol. Liq. **339**, 116829 (2021)

[30] Y. Li, S. Lan, Y. Liu, C. Cao, Z. Tang, D. Deng, F. Liu, H. Li, X. Fan, M. Zhu, Construction of ternary PEG200-based DESs lubrication systems via tailoring tribo-chemistry, Friction **12**, 655–669 (2024)

[31] A. Pandey, S. Pandey, Solvatochromic probe behavior within choline chloride-based deep eutectic solvents: effect of temperature and water, J. Phys. Chem. B **118**, 14652–14661 (2014)

[32] W.B. Hardy, I. Doubleday, Boundary lubrication—the paraffin series, Proc. A 1 March **100**, 550–574 (1922)

[33] D.A. Rigney, J.P. Hirth, Plastic deformation and sliding friction of metals, Wear **53**, 345–370 (1979)

[34] R. Natarajan, N. Palaniswamy, M. Natesan, XPS analysis of passive film on stainless steel, Open Corros. J. **2**, 114–124 (2009)

[35] C. Silva, F. Simon, P. Friedel, P. Poetschke, C. Zimmerer, Elucidating the chemistry behind the reduction of graphene oxide using a green approach with polydopamine, Nanomaterials **9**, 6 (2019)

[36] H. Yang, J. Bao, Y. Qi, J. Zhao, Y. Hu, W. Wu, X. Wu, D. Zhong, D. Huo, C. Hou, A disposable and sensitive non-enzymatic glucose sensor based on 3D graphene/Cu_2O modified carbon paper electrode, Anal. Chim. Acta. **1135**, 12–19 (2020)

[37] H. Zhang, Y. Huang, Z. Hu, C. Tong, Z. Zhang, S. Hu, Carbon dots codoped with nitrogen and sulfur are viable fluorescent probes for chromium(VI), Microchim. Acta **184**, 1547–1553 (2017)

[38] S. Chen, W. Zhao, S. Zhang, W Liu, Preparation, characterization and photocatalytic activity of N-containing ZnO powder, Chem. Eng. J. **148**, 263–269 (2009)

[39] Y. Qi, M. Yang, W. Xu, S. He, Y. Men, Natural polysaccharides-modified graphene oxide for adsorption of organic dyes from aqueous solutions, J. Colloid. Interf. Sci. **486**, 84–96 (2017)

[40] K. Shamsa, P.S.M. Rajaitha, S. Vinoth, C. Murugan, P. Rameshkumar, A. Pandikumar, In situ formed zinc oxide/graphitic carbon nitride nanohybrid for the electrochemical determination of 4-nitrophenol, Microchim. Acta **187**, 552 (2020)

[41] X. Bai, J. Liu, S. Wen, Y. Lin, Selective separation of chalcopyrite and pyrite using a novel organic depressant at low alkalinity, Miner. Eng. **185**, 107677 (2022)

[42] Y. Chen, B. Zeng, L. Lai, L. Luo, P. Xie, Q. Shao, Z. Liu, J. Ma, Sulfite activation using FeO as a source of ferrous ions for fluoxetine degradation: A collaborated experimental and DFT study, Chem. Eng. J. **441**, 135960 (2022)

[43] X. Tu, L. Xiao, Z. Cai, Z. Peng, D. Zeng, P. Ren, X. Zhao, X-ray photoelectron characterization of the chemical states and the natural oxidation behavior of TiC ceramics reinforced steel matrix composite after stabilizing heat treatments, Ceram. Int. **49**, 37316–37329 (2023)

[44] N.S. McIntyre, D.G. Zetaruk, X-ray photoelectron spectroscopic studies of iron oxides, Anal. Chem. **49**, 1521–1529 (1977)

[45] B.J. Tan, K.J. Klabunde, P.M.A. Sherwood, X-ray photoelectron spectroscopy studies of solvated metal atom dispersed catalysts. Monometallic iron and bimetallic iron-cobalt particles on alumina, Chem. Mater. **2**, 186–191 (1990)

[46] S.L. Wu, Z.D. Cui, F. He, Z.Q. Bai, S.L. Zhu, X.J. Yang, Characterization of the surface film formed from carbon dioxide corrosion on N80 steel, Mater. Lett. **58**, 1076–1081 (2004)

[47] L. Yuan, L. Liu, Y. Bai, J. Qin, M. Chen, F. Feng, A novel ratiometric fluorescent probe for detection of L-glutamic acid based on dual-emission carbon dots, Talanta **245**, 123416 (2022)

Cite this article as: L. Yuan, Z. Wang, C. Zhou, M. Fillon, M. Wang, Y. Wang, B. Wentao, W. Zhang, Hydrogen-bond regulated NADES lubricants enable ultra-low wear in high-speed ball screw pairs, Mechanics & Industry **27**, 18 (2026), https://doi.org/10.1051/meca/2026012